DOI:
10.1088/2399-6528/aace29

Document Version
Peer reviewed version

Quantum criticality associated with dimensional crossover in the iso-electronic series $Ca_{2-x}Sr_xRuO_4$

Quantum Criticality Associated with Dimensional Crossover in the Iso-electronic Series $Ca_{2-x}Sr_xRuO_4$

Swagata Acharya[1,2]

[1]Department of Physics, King's College London, London WC2R 2LS, United Kingdom

E-mail: swagata.acharya@kcl.ac.uk

[2]Department of Physics, Indian Institute of Technology, Kharagpur, Kharagpur 721302, India

Dibyendu Dey[2]

[2]Department of Physics, Indian Institute of Technology, Kharagpur, Kharagpur 721302, India

E-mail: dibyendu@phy.iitkgp.ernet.in

T. Maitra[3]

Department of Physics, Indian Institute of Technology, Roorkee, Roorkee 247667, India

E-mail: tulimfph@iitr.ac.in

A. Taraphder[2,4]

[2]Department of Physics, Indian Institute of Technology, Kharagpur, Kharagpur 721302, India

[4]Centre for Theoretical Studies, Indian Institute of Technology Kharagpur, Kharagpur 721302, India

E-mail: arghya@phy.iitkgp.ernet.in

Abstract. The iso-electronic series, $Ca_{2-x}Sr_xRuO_4$, is studied within the GGA (and spin-orbit coupled GGA) plus DMFT formalism using the hybridization expansion of continuous time Quantum Monte Carlo (CT-QMC) impurity solver. GGA+DMFT, along with CT-QMC impurity solver we used, provides insights into the retarded electronic correlations at finite temperatures. We use GGA+U and energy considerations at T=0 for complementary understanding of the ground state structural and electronic properties. While the dynamical correlations make Sr_2RuO_4 a Hund's metal, they drive Ca_2RuO_4 to a Mott insulating ground state. We study the single-particle and two-particle responses at three different points ($x = 2.0, 0.5, 0.0$) to understand the anomalous cross-over from Hund's metal ($x = 2.0$) to a Mott insulator ($x = 0$) and observe that a structural distortion is likely to be responsible. Further, dynamical correlations reveal that the band-width (W) of the Hund's metal is larger than its effective local Hubbard U, and a finite Hund's coupling J_H helps it remain in a bad metallic and nearly spin-frozen state over a large temperature range. Ca_2RuO_4,

though, is driven to the proximity of a Mott transition by the narrowing of band width ($U/W > 1.5$). We show that there is a critical end point of second-order structural transition at $x = 0.5$, where spin fluctuations become critical and follow the scaling of local quantum criticality. We argue that this critical end point of quasi-3D nature is associated with an effective dimensional cross-over from the quasi-2D structures of $x = 2.0$ and $x = 0.0$ end-members. Finally we draw an electronic and magnetic phase diagram in T-x plane with these novel inputs, with a fan like region starting from the quantum critical end point at $x = 0.5$.

Submitted to:

PACS numbers: 71.30.+h 71.20.-b 74.70.Pq 71.27.+a

1. Introduction

Partially filled d- and f-electron systems are usually correlated electronic materials and the proximity of a Mott transition makes some of these materials rather interesting (1; 2). Mott metal-insulator (MIT) transition, heavy fermion behaviour, unconventional high-T_c superconductivity, colossal magnetoresistance are some of the dramatic phenomena arising, solely or partly, due to strong local correlations. They can fall in either of the effective single or multi-orbital (MO) framework depending on the active orbitals at the Fermi level. There are, however, MO systems such as Ruthenates (3; 4), iron pnictides (5; 6) and chalcogenides (7) which are strongly correlated metals not at the border of a Mott insulating phase. The role of Hund's coupling (8; 9; 10; 11; 12) in single and two-particle responses in many such MO materials have now been extensively investigated. The Hund's coupling leads to an exponential suppression of the coherence scale of a MO metal and leads to a large spin-frozen non Fermi-liquid phase. Hund's coupling has profound and distinct effects on spin, orbital and charge degrees of freedom. Nearly degenerate d-orbital systems away from half-filling are driven away from the Mott transition as the Hund's coupling prevents opening of a dynamical charge gap. These disparate, double-faced nature of Hund's coupling in controlling the properties of a correlated metal earned considerable recent interest (13; 14).

Ruthenates appear to be tailor-made for investigating the role of Hund's coupling at and away from half-filling. Being 4d-materials, the electrons are less localized than their 3d-counterparts and are not as strongly correlated; they are relatively far from the Mottness. The symmetry of the Ru t_{2g} orbitals favors a large hybridization with O p orbitals and leads to a large splitting between the t_{2g} and e_g orbitals. This, in turn, populates the 3 t_{2g} orbitals with 4 electrons and leads to a lower spin state than that of isoelectronic Manganites (with 3d valence states). An extensive study on the isoelectronic Ruthenates, $CaRuO_3$, $SrRuO_3$ (15; 16; 17; 18) and $BaRuO_3$ (19; 20) (Ru^{4+}, $4d^4$ electron configuration), reveals that all of them can be regarded as prototypical examples of Hund's metals with nearly spin-frozen state. The role of Van Hove singularity and J_H have been extensively studied (19) in these compounds to rationalize their electronic and magnetic properties. Reasonable values of U and J have been gleaned (16; 19; 20) on these materials from experimental single and two-particle features. The ground states and the finite temperature non-Fermi-liquid states are described within three-orbital DFT+DMFT framework with such values of U and J_H. Large mass enhancement factors (16), substantial increment in the linear specific heat coefficient γ and absence of a Mott insulating phase are common to all these three materials. The difference between them, however, involves the nature of magnetic ground states and the *Ru-O-Ru* bond-angles. The smaller *Ca* ion leads to a larger rhombohedral distortion (*Ru-O-Ru* bond-angles is 150°) of the lattice than that of the rhombohedral $GdFeO_3$ structure of $SrRuO_3$ (*Ru-O-Ru* bond-angles is 163°). The bandwidth of $CaRuO_3$ reduces substantially and the density of states at the Fermi level diminishes leading to a (non-ferromagnetic) magnetic ground state unlike $SrRuO_3$. On

the other hand $BaRuO_3$ has no $GdFeO_3$ distortions with *Ru-O-Ru* bond-angle 180° and is perfectly cubic.

This scenario, however, changes significantly for $4d^4$ (Ru^{4+}) Ruthenates, Sr_2RuO_4 and Ca_2RuO_4. Sr_2RuO_4 is a *p*-wave superconductor (though the symmetry may change under strain (21)) below 1.5K and a Fermi liquid metal at low temperatures, between 1.5 K and 25 K. The isoelectronic member at the other end of the series, Ca_2RuO_4, is a Mott insulator with an antiferromagnetic (AFM) ground state for $T < 113K$, a paramagnet state for $T < 356K$ (22) and a bad metal above $356K$ (23) all the way up to about 1300K. Recent studies on Sr_2RuO_4 have established that it is a non-Fermi-liquid above 25K, with Curie-Weiss susceptibility, and can be explained satisfactorily within Hund's metal framework with $U = 2.3eV$ and $J = 0.4eV$ (24). The interplay of SOC and Hund's correlations (25; 26) govern most of its properties. While the Hund's metal picture of this compound seems well settled, it or may not be entirely true in case of Ca_2RuO_4 (27). A recent experimental work finds signatures of Hund's coupling in the Mott insulator Ca_2RuO_4 (28). The values of U and J for this compound need to be settled within a $DFT + DMFT$ analysis by putting the single and two-particle responses to test against the experimental findings. At the same time it is interesting to investigate why, having all the required features of being a tailor-made Hund's metal (finite and large J, not half-filled), the system chooses to become a correlated (Mott) insulator instead. One relevant question is, whether the smaller Ca ions lead to a larger distortion of the octahedra. Existing literature suggests that the strong distortion of RuO_6 octahedra, associated with rotation, tilting and flattening respectively, drives the ferro- or anti-ferro-magnetic (29) nature of the ground states of $Ca_{2-x}Sr_xRuO_4$ (30) and stabilizes them, while in case of $CaRuO_3$ the distortion is comparatively less because there is only one Ca ion in the unit cell, instead of two for Ca_2RuO_4.

This "large distortion" argument immediately raises questions: is there an effective dimensional cross-over across the series as one starts replacing Sr by Ca? As we move across the series ($x = 2$ to $x = 0$), is some kind of a quantum critical point encountered? How do the local spin fluctuations evolve across the series? Are they critical at any x? Keeping these questions in mind, we would like to focus on the recent magnetic phase diagram for the series (31). Our aim is to verify and update the magnetic and electronic phase diagram from our theoretical analysis, systematically analyzing the structural distortion, dimensional crossover, spin fluctuations and possible local quantum criticality.

2. Methods

Although a substantial number of experiments to probe charge, spin and orbital sectors across the phase diagram has been carried out, systematic theoretical studies are lacking. We perform a first-principles calculations (GGA and spin-orbit (SO) coupled GGA) followed by dynamical mean field theory, using state-of-the-art hybridization expansion of 'exact' continuous time quantum Monte-Carlo (CT-QMC) impurity solver (32; 33)

as implemented in ALPS (34). We probe both single- and two-particle local static and dynamic responses for this series. We first perform ab-initio density functional theory calculations within GGA and GGA+SO for Sr_2RuO_4 using the full potential linearized augmented plane-wave (FP-LAPW) method as implemented in the WIEN2k code(35). DFT calculations are performed using experimental structural parameters(36; 37; 22). At the outset we discuss the results from only GGA calculations (without SO). We perform Wannierization of the Wien2k output bands around the Fermi level via interface programs like Wannier90 (38), WIEN2Wannier (39). This, in turn, gives us the Wannier orbitals around the Fermi level which serve as inputs to the DMFT self-consistency calculation. Similar procedure is followed subsequently for the calculations of $Ca_{1.5}Sr_{0.5}RuO_4$ and Ca_2RuO_4. However, SO-coupled GGA has not been performed for these two compounds as discussed later. From the first-principles calculations, we would also try to address the role of van Hove singularities, effective band widths (of itinerant bands crossing the Fermi level), and Ru-$4d - t_{2g}$-O-$2p$ hybridization in tuning the local electronic and magnetic properties of this series.

We then rationalize our choices of U and J for different x, and the role of local correlations in modifying the low energy single- and two-particle responses, using DMFT. The double counting term is $E_{dc} = U(n - 1/2) - J(n/2 - 1/2)$, where n is the total occupation of the Wannier projected $Ru - d$ orbitals. Some standard choices of CT-QMC parameters that ensure proper convergence of data are : total number of Monte Carlo steps per core 100000000, warmup number of QMC steps 5000000, and the global flip 200000. However, apart from these, the convergence criteria imposed on the occupancy is 10^{-6}. The convergence in occupancy ensures that the dynamic quantities like hybridization, local single particle Green's function and self energies also converge properly. At the end we also check that the chemical potential converges within 10^{-6} precision after several (10-15) DMFT iterations.

3. Results and Discussion

3.1. Sr_2RuO_4: DFT+DMFT

DFT (GGA) bands and Wannier fit

The delocalized Ru $4d$-orbitals and a large Ru atomic weight (Z=44) make SO coupling relevant in these materials (as the SO coupling strength $\sim Z^4$). Whether a p-wave triplet instability, derived from a momentum-dependent SO coupling, drives a pairing instability in the material at low temperatures has been debated over last two decades (3; 40; 41; 42). We are, however, interested in probing the 'normal state'; in particular, the role of SO coupling on single- and two-particle dynamical responses down to low temperatures (we could reach $19K$), well inside the normal phase. We discuss below the results we obtained from DFT+DMFT calculations on Sr_2RuO_4 without and with SO coupling. The first-principles calculations within GGA and subsequent Wannier fit lead us to 3 active orbitals at the Fermi level (Fig 1(a)). These orbitals are

primarily derived from *Ru* $4d$ states and have reasonably large hybridization with the $O\,p$ states at the Fermi level. The hybridization of the *Ru*-$4d$ and apical Oxygens are predominantly between *Ru*-$4d$ d_{xz}, d_{yz} and *O*-$2p$ p_x, p_y states. The p_y, p_z orbitals of the Oxygens in the RuO_2 plane hybridize with the *Ru* d_{xy} and d_{yz} orbitals respectively. The latter kind of hybridization is more favorable, and is reflected in the energy range of 300 meV about the Fermi energy, while the earlier one is relevant away from the Fermi level ($\sim$ 1 eV). These hybridizations lead to dispersive electrons in the RuO_6 octahedral geometry. We perform Wannier fits to these three bands (of mixed *O*-$2p$ – *Ru*-$4d$ character). In Fig. 1(a) the character of the Wannier bands are shown. The three figures, Fig. 1(b), (c) and (d), respectively, bring out the d_{xy}, d_{xz} and d_{yz} contributions to the bands crossing the Fermi level. Although the original bands are now rotated and mixed, as is apparent in Fig 1, the band characterization allows us to refer to them as nominally d_{xy}, d_{xz}, d_{yz} respectively. Subsequently we take these Wannier bands as input of our DMFT calculations and refer to them as such for the rest of the discussion. We choose a value U=2.30 eV and J_H=0.40 eV from the literature (24) for Sr_2RuO_4. The choice is motivated by the fact that it predicts the experimentally derived values of local moment and quasi-particle weight over a wide range of temperature quite well. We start by showing the crystal structure of Sr_2RuO_4 with (space-group I4/mmm) tetragonal structure (a=3.8606 A^0 and c=12.70658 A^0) in Fig. 2(a).

CT-QMC+DMFT: Single-particle Green's function and self energy, two-particle spin susceptibility

Imaginary parts of the single-particle self-energy, Im$\Sigma(i\omega)$ (Fig. 2(b)), and the Green's function, Im$G(i\omega)$, are plotted for temperatures in a range between 116K to 19K for individual orbitals. The intercept of Im$\Sigma(i\omega)$ at ω=0 and hence, the scattering rate reduces monotonically (Fig 2(c)) and approaches zero with lowering temperatures. Im$G(i\omega)$ also becomes more coherent as the temperature is lowered: the systematic retrieval of coherence is evident from Im$\Sigma(i\omega)$, and Im$G(i\omega)$. We fit Im$\Sigma(i\omega)$ to a fourth order polynomial in $i\omega$. The mass enhancement, related to the coefficient (s_1) of the linear term in the expansion $m^*/m = 1 + s_1$ (43), increases with lowering of temperature (Fig. 2(c)). It can be seen that the xy orbital has a larger mass enhancement than the xz and yz orbitals (13; 16), and concomitantly, the magnitude of the intercept of Im$\Sigma(i\omega)$ at ω=0 for xy orbital is larger than that for the other two (Fig. 2(c)). The m^*/m for d_{xy} is 5.8 and for d_{xz}, d_{yz} 4.5, in excellent agreement with experiments and earlier theoretical studies.

To unravel the nature of spin fluctuations, we apply a small uniform field (h) and measure the magnetization (M) over a range of temperatures. We plot the inverse of the uniform spin susceptibility ($\chi^{-1} = h/M$) as a function of temperature between 290 K and 29 K and extract the critical temperature(T_c) for the magnetic transition (from $\chi^{-1} \propto T - T_c$, Fig. 2(d)). For Sr_2RuO_4 T_c is -16.6 K, indicating pre-dominant anti-ferromagnetic spin fluctuations. On the other hand, the non-Fermi-liquid to Fermi-

liquid cross-over around 25K, observed in experiments, cannot be demonstrated cleanly from these results. We switch over to static and dynamic spin susceptibilities to glean whether the incoherence to coherence cross-over is reflected in the two-particle sector: it often happens that a low-energy single-particle description is not adequate to trace such cross-over scales associated with multi-particle dynamics (44; 45). The local dynamic spin susceptibilities ($\chi_s(\tau)$) (46; 47) have been plotted against τ (Matsubara time) for a large range of temperature (Fig. 2(e)). We also calculate the time-integrated local spin susceptibility ($\chi_s(T)$) (Fig. 2(f)). $\chi_s(\tau)$ below $\sim 29K$ seems to have a zero intercept at $\tau = \beta/2$ and a τ^2 behavior around $\tau = \beta/2$, while for higher temperatures the intercept is finite and large and increases with a rise in temperature. $\chi_s(\tau)$ also deviates from a low-energy τ^2 behavior with increasing temperatures. To add to that, $\chi_s(T)$ clearly shows a deviation from its high temperature Curie-Weiss behaviour at $\sim 41K$ (Fig. 2(f)). Although the low temperature behavior (as shown in inset of Fig. 2(f)) of $\chi_s(T)$ below 41K is not Pauli-like (indicating the spins are not quenched completely below this temperature), the strong deviation from Curie-Weiss behavior is a signature of the emergence of a low temperature coherence scale.

At this point we do further calculations by incorporating SO coupling to elucidate the presence of any such crossover scale. From GGA+SO calculations we find that the orbital degeneracies are lifted at different k-points across the Brillouin zone by different amounts (not shown here). The maximum value of SO splitting is $\sim$ 130 meV while it is negligible at some symmetry points. The effect of SO, however, can hardly be realized by looking at the momentum-integrated density of states of Sr_2RuO_4. We find lesser hybridization between the apical Oxygens and $Ru\,4d\,t_{2g}$ orbitals. We identify the bands active at the Fermi level and perform the Wannierization. Similar to our previous calculations, the Wannier fit orbitals have predominant contributions from $Ru-d_{xy}, d_{xz}, d_{yz}$ orbitals, however, now we have 6 spin-orbitals instead of three orbitals with spin degeneracy.

In-plane and out-of-plane hopping

The values of real space hopping, gleaned from Wannierization, are also suggestive. The relative magnitudes of the in-plane and out-of-plane hopping elements provide insight into the effective dimensionality of the material. The c/a ratio for Sr_2RuO_4 is 3.294 and the in-plane hopping elements of the itinerant electrons are nearly an order of magnitude larger than their out of plane counterparts (Fig 3(a)). The system is quasi-$2D$ in this case, supported also by a large resistivity anisotropy ratio (49; 48) ($\rho_c/\rho_{ab} \sim 200$) and lesser hybridization between the apical Oxygens and $Ru\,4d\,t_{2g}$ orbitals.

CT-QMC+DMFT (with SO): Single-particle Green's function and self energy, two-particle spin susceptibility

We perform our DMFT calculations using these SO-coupled orbitals. The DMFT self-energies (Fig 3(b)) have similar qualitative features as in without-SO calculation, though

the details are very different now. Here again the intercept of Im$\Sigma(i\omega)$ (Fig 3(c)) at ω=0 decreases with increasing temperature, but the drop is sharper and non-monotonic across 40 K. The m^*/m is, in turn, found to increase sharply across it (Fig 3(c)). We find that the scattering rate Γ (as can be derived from the intercept of the -Im$\Sigma(i\omega)$, $\Gamma = -ZIm\Sigma(\omega = 0)$) crosses over from a high temperature linear (fitted exponent 1.02) to a lower temperature quadratic (fitted exponent 2.12) in temperature behavior in Fig. 3(d). This clearly marks the advent of a FL like phase at lower temperatures. Both Im$\Sigma(i\omega)$ and Im$G(i\omega)$ can be found to have sharp change of slope below ω=0.03 eV (Fig 3(b)), marking the emergence of of coherence at lower temperatures. At this point we look at the two-particle responses. The $\chi_s(\tau)$ (Fig 3(e)) shows Fermi-liquid features, with a $\tau = \beta/2$ intercept ~ 0 and τ^2 behavior at low energies, below 23K. The $\chi_s(T)$ (Fig 3(f)) seems to be deviating from the high temperature Curie-Weiss behavior precisely below the same scale of T, marking the emergence of coherence in the system. Hence, the scenario with SO is distinctly different from the scenario without SO. With SO included, both the single and two-particle static and dynamic responses register the emergence of coherence quite consistently at lower temperatures. However, the Fermi surface provides more insight into the low energy excitations of the material. We find (Fig. 4) that d_{xz} and d_{yz} Fermi surfaces are effectively one dimensional and d_{xy} Fermi surface is two dimensional, making the whole system quasi 2D which is in consistency with our estimation of Wannier hopping parameters. The replacement of Sr by a smaller cation Ca suggests the possibility of a dimensional cross-over, and such a cross-over could encounter a structural or magnetic critical point.

3.2. $Ca_{1.5}Sr_{0.5}RuO_4$: DFT + DMFT

DFT (GGA) bands and Wannier fit

Though the crystal symmetry remains tetragonal (Fig 5), RuO_6 octahedron is distorted considerably as Ca cations replace Sr. The distortion takes place in steps (50; 51): first occurs a rotation of the octahedra about the c axis and then a tilt of the octahedra, followed finally by a flattening of it. $Ca_{1.5}Sr_{0.5}RuO_4$ undergoes the first kind of distortion, starting from a nearly clean undistorted RuO_6 octahedra in Sr_2RuO_4. The GGA calculations allow us to glean the primary changes in its band structure thereon as shown in Fig. 6. The Ru-4d bands get significantly narrowed in this case compared to Sr_2RuO_4. Further, the distortions present in the RuO_6 octahedra cause a small admixture of d_{z^2} and $d_{x^2-y^2}$ (so-called e_g states) characters in the DOS around the Fermi level which are otherwise primarily of d_{xy}, d_{yz} and d_{zx} characters (known as t_{2g} states). The d_{xy} orbital is the majority contributor to DOS, with a sharp Van-Hove like feature within an energy range of 50 meV of the Fermi level. The d_{yz} and d_{zx} orbitals are secondary contributors. While p_y and p_z orbitals of in plane (RuO_2 plane) Oxygens hybridize strongly with the Ru 4d at the Fermi level, p_x and p_y orbitals of apical Oxygen hybridizes strongly with the Ru 4d nearly 700-800 meV away from the Fermi level. However, Wannierization and band characterization suggest that the

Wannier fit bands can be identified (similar to Sr_2RuO_4) as predominantly d_{xy}, d_{xz}, d_{yz}-derived ones as shown in Fig. 6. The sharp Van-Hove feature close to the Fermi surface and the narrow band-width of the *Ru d* orbitals already place the material close to a ferromagnetic Stoner instability.

In-plane and out-of-plane hopping

We look at the in-plane and out-of-plane Wannier hopping amplitudes. The c/a ratio turns out to be 3.30 which is almost similar to Sr_2RuO_4. What is interesting is the ratio of the in-plane and out-of-plane hopping amplitudes. The out-of-plane hopping along the z direction is not suppressed at all: both in-plane and out-of-plane components (Fig 7(a)) are nearly of the same order of magnitude. It would be relevant to reflect upon the lattice distortions at this point. As the Sr gets replaced by Ca the RuO_6 octahedron starts to rotate with an angle ϕ about the c axis and reaches a maximum of 12.78° at $x = 0.5$. However, the tilting (θ) of RuO_6 around an axis parallel to the edge of octahedral basal plane remains 0 till this point. It is also noteworthy that the degree of flattening λ along the c axis remains almost unchanged between $x = 2.0$ and $x = 0.5$. The effective three dimensional nature of the electron hopping suggests that, in spite of having a similar c/a ratio the $x = 0.5$ material has $3D$ itinerant electrons, unlike its $x = 2.0$ counterpart.

CT-QMC+DMFT: Single-particle Green's function and self energy

We use these Wannier-fit (using the three dt_{2g} Wannier orbitals) bands as inputs for DMFT. The DMFT calculations are performed with $U = 3.0eV$ and $J_H = 0.6eV$. The rationale behind these parameter values is again the same − the local static quantities are well-reproduced for a range of temperatures with these parameters. These numbers are larger than the corresponding numbers for Sr_2RuO_4, for the width of the bands crossing the Fermi level has decreased now (smaller Ca cations replacing bigger Sr). $\mathrm{Im}\Sigma(i\omega)$ and $\mathrm{Im}G(i\omega)$ are plotted as functions of $i\omega$ in Fig 7(b) and they show tendencies towards enhanced coherence as temperatures go down. However, unlike Sr_2RuO_4, the material here remains in-coherent down to the lowest temperatures probed. The intercept, shown in Fig 7(c), of $\mathrm{Im}\Sigma(i\omega)$ at ω=0 is nearly independent of temperature and remains large and finite down to the lowest temperature studied. In the inset of Fig 8 (upper panel) we show the scattering rate Γ (as derived from the intercept of the -$\mathrm{Im}\Sigma(\omega = 0), \Gamma = -ZIm\Sigma(\omega = 0)$) as a function of temperature between 58 K and 290 K. We find that the scattering rate has a thermal exponent 0.18, far from the quadratic Fermi liquid limit. Moreover, the extremely weakly temperature-dependent scattering rate suggests that the low energy scattering of the system is incoherent NFL-like: the temperature does not have significant effect on the nearly spin-frozen metallic state (20). Although these results clearly show that the single-particle response of the system is not fully coherent, the identification of an NFL needs analysis of the two-particle responses. Further, the scaling features of local spin susceptibility will allow us

to quantify the local moment fluctuations, important for identification of a local NFL.

Orbital selectivity and spin fluctuations

We analytically continue the single particle Green's functions using maxmimum entropy method (MEM) (52). The analytically continued, orbitally projected local density of states show that $Ca_{1.5}Sr_{0.5}RuO_4$ has orbital-selective quasi-particle response. The d_{xz}, d_{yz} orbitals have well-defined low-energy quasiparticle spectra, while the d_{xy} orbital has pseudogapped single-particle spectrum (Fig 8(upper panel). The orbital-selective nature of the $\mathrm{Im}\Sigma(i\omega)$ can be gleaned from the fact that d_{xy} orbital has a very small intercept at ω=0 compared to d_{xz} and d_{yz} orbitals, but the mass enhancement factors for the d_{xz} and d_{yz} orbitals steadily decrease with lower temperatures (Fig 7(c)). The dependence is not as monotonic for d_{xy} orbital. This can again be corroborated by the orbitally projected density of states: d_{xz} and d_{yz} orbitals have coherent features while the d_{xy} orbital is pseudo-gapped as shown in Fig. 8.

To glean the nature of spin fluctuations, we apply a small uniform field (h) and measure the magnetization (M) over a range of temperatures. We plot the inverse of the uniform spin susceptibility (χ^{-1}) as a function of temperature and extract the critical temperature (T_c) for the magnetic transition from a Curie Law fit (Fig. 7(d)). For $Ca_{1.5}Sr_{0.5}RuO_4$ T_c it is positive 0.59 K. This number for T_c is weakly positive. What is, however, interesting is its increment with respect to two end points $x = 0.0, 2.0$ (the value and the sign for T_c for $x = 0$ is discussed later and at $x = 2.0$ T_c is -16.6 K). And finally, $\chi_s(T)$ (Fig 7(f)) for this material, is more than an order of magnitude larger (30) than $\chi_s(T)$ for Sr_2RuO_4 in this temperature range. Moreover, as we already discussed, extremely weak temperature dependence of the scattering rate also suggests that the low energy excitations of the system are NFL-like, a nearly spin-frozen state. All these quantities ($T_c > 0$, order of magnitude enhanced $\chi_s(T)$ and very weak temperature dependence of scattering rate), suggest that the system tries to stabilize a large local moment while it has ferromagnetic fluctuations. We note with interest that $\chi_s(\tau)$ has different functional dependencies on τ at high (between 600K to 120K) and low (below 120K) temperatures. The high-temperature $\chi_s(\tau)$ suggests that even at low energies the spin is completely unquenched – a partial quenching of spins begins below 120K. Thereafter the spin quenching increases as the temperature is lowered. But $\chi_s(T)$ in Fig 7(f) suggests that the response remains Curie-Weiss-like down to the lowest temperatures accessed within our CT-QMC, indicating that local moment survives at the lowest temperatures.

Local critical fluctuations at finite temperature from a critical end-point

Few concrete observations may be made at this point. First, both $ImG(\tau)/ImG(\beta/2)$ and $\chi_s(\tau)/\chi_s(\beta/2)$ scale with τ/β (Fig 7e) which suggests that temperature is the only scale in this parameter regime. The scaling functional form is $Sin(\pi\tau/\beta)^{(\alpha-1)}$ (53) with α=0.10 and hence the criticality is strictly local. As the $\chi_s(\tau)$ is analytically

continued, using maximum entropy method (MEM) (52), we find that different curves for $\mathrm{Im}\chi_s(\omega,T)/\chi_s(T)$ (Fig 8(lower panel)) have perfect collapse on each other up to ω/T $\sim$1.0 over a range of temperatures. This thermal scaling collapse on real frequencies further substantiates the suggestion that $Ca_{1.5}Sr_{0.5}RuO_4$ is in the proximity of a quantum critical point. These signatures indicate a strong quantum critical fluctuation at $x = 0.5$ at temperatures below our reach in CT-QMC. This could well be a critical end point ($T = 0, x = 0.5$), as there is no experimentally reported structural transition either suppressing or facilitating the critical ferromagnetic fluctuation at this point (37). The orbital selective pseudogapped (Fig 7b, 8) (53) density of states, non-Fermi-liquid self-energy response, nearly spin-frozen scattering rate also support the quantum criticality scenario, which is shown to exist in different contexts (54; 55; 56; 57) in the literature with similar single-particle responses. However, a recent report (31) suggests the presence of a very low temperature cluster glass phase at $x = 0.5$, which may obscure access to this point.

It is worth noting that c/a ratio can not be the lone parameter deciding the effective dimensionality of a bulk single crystal. The distortion-induced changes in the *Ru d* and apical *O p* hybridization scales are equally important in determining the effective dimensionality. The Fermi surfaces (Fig 9) for $x = 0.5$ clearly show that they have significant dispersion along the z direction (58; 59) unlike the Fermi surfaces for Sr_2RuO_4 which was quasi-2D. This effective dimensionality, critical ferromagnetic spin fluctuations, finite temperature Curie-Weiss spin susceptibility, positive θ_c, finite temperature scaling collapse of dynamic spin susceptibilities, and absence of any magnetic, orbital or charge ordering down to lowest temperatures indicate that $x = 0.5$ is critical. This is again of great interest, as it is already reported in literature (37) that there is a $T - x$ line that separates the $Ca_{2-x}Sr_xRuO_4$ phase diagram in to two regions; one with two fold in-plane susceptibility-anisotropy (at lower x below x=0.5) (60) and the other region, $x > 0.5$, without any anisotropy. This suggests that there is reasonably compelling evidence that $x = 0.5$ could well be a quantum critical end point of a second-order structural transition. Having observed the criticality at $x = 0.5$, a moot question is: what would be the effect of the critical fluctuations at lower x? We investigate Ca_2RuO_4 now on these lines.

3.3. Ca_2RuO_4: DFT + DMFT

DFT (GGA) bands and Wannier fit

As experimental evidences suggest (60; 30), Ca_2RuO_4 has an AFM Mott insulating state below 113K. Between 356K and 113K it is a paramagnetic Mott insulator and above 356K, a paramagnetic bad metal. The metal to Mott insulator transition at 356K is associated with a structural transition from an *L-Pbca* (Fig 10) to *S-Pbca* structure. We first do GGA calculations using L-Pbca structural inputs from experiments(22), perform Wannierization, apply local correlations within DMFT scheme on Wannier-fit orbitals (Fig 11) and look for a Mott metal-insulator transition. In this case all the

d orbitals have substantial contributions to the DOS at the Fermi level due to large distortions causing stronger admixture of these orbitals. There are sharp Van-Hove features near the Fermi level, but they are farther from the Fermi level than those in $Ca_{1.5}Sr_{0.5}RuO_4$. However, the bandwidth for the dispersive d orbitals are even lower in this case than the $x = 0.5$ material. The highly distorted octahedron admits strong hybridization between all $Ru\,d$ orbitals and $O\,p$ orbitals: the apical Oxygen p_x, p_z and in-plane Oxygen p_x, p_y, p_z have sufficient hybridization with $Ru\,d$ orbitals. All these facts put together, the L-Pbca structure here has an intrinsic tendency towards nesting and thence antiferromagnetic fluctuations, which stabilize a low temperature AFM ground state with energy gain $\sim t^2/U$. The L-Pbca structural details, however, do not explain why it should become a Mott insulator below 356K. It is often suggested in the literature (27) that the L-Pbca to S-Pbca structural transition drives the Mott transition associated with an orbital ordering (60) across 356 K. However, Gorelov et al., (27) do not get any orbital selective Mott transition for the L-Pbca phase down to 300 K in their analysis. After Wannierization of the GGA bands for L-Pbca, we employ local correlations within DMFT+CT-QMC framework and try to see if there is Mott transition somewhere lower temperatures. Subsequently the questions of interest are: what is the nature of the Mott insulator? Re-paraphrasing, whether all the active orbitals become Mott insulating or is there orbital selectivity? How do the DMFT results compare with available ARPES data? And finally, is the desired Mott insulating state recovered at 356K if the S-Pbca structure is subjected to local correlations within GGA+U?

In-plane and out-of-plane hopping

Before addressing those issues, it is also useful to note the relative values of the in-plane and out-of-plane effective hopping for Ca_2RuO_4 (Fig 12(a)). Figure 12(a) clearly shows that, even inside the L-Pbca phase, just above the Mott transition, c/a is ~ 2.06 and the out of plane hopping is significantly suppressed in comparison to the in-plane hopping, t_c/t_{ab} ratio being 0.3 at $x = 0$. The nearly $2D$ nature (60; 61; 62) of the Ca_2RuO_4 bulk single crystal is in marked contrast to its $x = 0.5$ counterpart, as far as the effective dimensionality (measured by t_c/t_{ab} ratio ~ 1 and c/a ratio 3.3 for $x = 0.5$) is concerned.

CT-QMC+DMFT: Single-particle Green's function and self energy, two-particle spin susceptibility

We choose $U = 3.1eV$ and $J_H = 0.7eV$ (27) for the present analysis. As the temperature is lowered from 1000K to 360K, we observe that unlike the rest of the materials that we have studied, there is no monotonic tendency for $\mathrm{Im}\Sigma(i\omega)$ and $\mathrm{Im}G(i\omega)$ (Fig 12(b)) towards coherence. Rather, orbital specific loss of coherence can be clearly observed by lowering the temperature (63; 64). Finally it is found that the d_{xy} orbital becomes Mott gapped with consistent singular low energy features in the $\mathrm{Im}\Sigma(i\omega)$ below 250K. The charge gap is clearly orbital selective (64) in nature, as other orbitals remain metallic

as far as their single-particle dynamic responses are concerned, down to the lowest temperature. One important point is that, for $Ca_{1.5}Sr_{0.5}RuO_4$, the orbital with primarily d_{xy} character was the one that became pseudogapped and for $x = 2.0$ the orbital with major contribution from d_{xy} becomes Mott gapped below 250K (Fig 12(c)). The critical Mott temperature, as is apparent, is much lower than the experimentally realised 356K scale.

ARPES studies do suggest (64; 63) that the transition is orbital selective in nature, although the absence of orbital-selective Mott nature is also supported by one ARPES study (65) and one theoretical study (27). Not much can, however, be concluded from the intercept of $\mathrm{Im}\Sigma(i\omega)$ at $i\omega = 0$ and the orbital specific mass enhancement factors (Fig 12(d)), except for the fact that the intercept becomes extremely large in the proximity of Mott transition. We find that $\mathrm{Im}\Sigma(i\omega)$ becomes singular below a critical temperature, and the quasi-particle description becomes somewhat untenable.

In the two-particle sector, the temperature dependence of $\chi_s(\tau)$ suggests that the local moment remains unquenched at all energy scales in the temperature range between 800K to 400K. The local moment remains large and finite down to the Mott critical temperature ($T_{c,Mott}$), however, the local susceptibility behavior just above 356 K deviates slightly from Curie-Weiss (Fig 12(e)). The high temperature $\chi_s(T)$ follows Curie-Weiss law as shown in main panel and inset of Fig 12(e). The extracted uniform spin susceptibility (Fig. 12(f)) shows that T_c is negative (-21.48 K),i.e., the antiferromagnetic fluctuation is prevalent in Ca_2RuO_4. It is well known in the literature that the system does have an antiferromagnetic insulating ground state below 113 K. Clearly, our local analysis correctly predicts the nature of local instabilities in the excitation spectrum.

It is not possible to properly trace a self-consistent Mott metal-insulator transition across 356K within our local analysis, as it does not include the structural transition (27) (at 356K), role of phonons and the likelihood of an orbital ordering (66; 67; 68). We start with a high temperature L-Pbca structure, cool the system down to 250K and observe that there is a possibility of an orbital selective Mott transition around this temperature. Next we perform a GGA calculation with the S-Pbca structure and include local Hubbard correlations within the GGA+U framework. We find that there is indeed a Mott transition with S-Pbca structure.

This Mott transition, via the structural transition, has already been studied in literature (27). It is interesting to compare the relative scales of local correlations U and J_H with the band-widths of the dispersive electronic orbitals around the Fermi level across the series. Sr_2RuO_4 has a larger bandwidth (W), roughly 2.8 eV, and the U/W ratio is about 0.89, while J_H/W is 0.18. The Mott criteria suggests that U/W has to be of order one or more to facilitate a Mott transition. A comparatively large J_H/W, in addition, takes the system away from the proximity of a Mott transition, as the system is less than half filled. For Ca_2RuO_4 the effective bandwidth of the bands crossing the Fermi level is only $\sim 1eV$. The large distortion of the octahedra narrows the dt_{2g} bands significantly and leads to an increment in the U/W, driving the material

to the proximity of a Mott transition via a structural transition. This effectively pushes the system away from the Hund's limit and puts it in the Mott limit. The L-Pbca to S-Pbca transition is again associated with a flattening of the octahedra with nearly 10% decrease in c/a ratio at 356 K. While the flattening parameter λ shows a reduction from 1.07 to 0.96 (51; 30), the rotation angle remains nearly fixed between $x = 0.5$ and $x = 0.0$. However the tilting angle θ changes by 12° between $x = 0.5$ and $x = 0.0$.

4. A GGA+U insight into the ground state properties across x=0.5

The impurity solver CT-QMC solves the impurity correlated Hamiltonian by sampling all essential fermionic diagrams at finite temperatures and those are 'exact' within a local-approximation. However, being a stochastic finite-T solver, it cannot access the ground state properties. GGA+U, instead, can be used as a complementary technique at the ground state (T=0) to see how much of the physics observed at finite temperatures with CT-QMC+DMFT has their roots at T=0. We have performed GGA+U calculations by varying c/a ratio from -5% to +5% around the experimental c/a for x=0.5 structure. We note that according to the experimental phase diagram (60), at lower temperatures there is no metal-insulator (MIT) transition across x=0.5 and the system remains metallic with $I4_1/acd$ symmetry for the entire range $0.2 < x < 1.5$ (27). However, there is a magnetic phase transition (ferromagnetic to paramagnetic (PM)) at low temperature across x=0.5 ($0.2 < x < 0.5$ the system is ferromagnetic metal, and $x > 0.5$ it is paramagnetic metal). System shows AFM insulating behavior at low temperatures only in the doping range $0 \leq x \leq 0.2$ (S-Pbca structure).

x	Spin Config.	Energy/cell (Ry)
0	FM	-49551.5344
	AFM	-49551.5399
	NM	-49551.4991
0.5	FM	-59549.2905
	AFM	-59549.2734
	NM	-59549.2694

Table 1. Calculated total energies for three different spin configurations (Ferromagnetic (FM), Antiferromagnetic (AFM) and Non-magnetic (NM)) for x=0.0 and x=0.5 structures.

In order to find out if GGA+U can correctly reproduce the ground state magnetic and transport properties of Ca_2RuO_4 (x=0) and x=0.5 doped structure where the experimental ground state for the former is antiferromagnetic insulator and that of the latter is ferromagnetic metal, we have carried out GGA+U calculations for both the compounds considering their low temperature experimental structures (30). U_{eff} (U-J) = 2.5 eV has been considered for Ru in our calculations. We observe that AFM

is the ground state magnetic configuration for the parent compound whereas FM is the ground state in case of x=0.5 (see 1). We can also see from Fig. 13(a) that there is a band gap ($\approx$ 0.8 eV) in the density of states (DOS) for Ca_2RuO_4 compound whereas, $Ca_{1.5}Sr_{0.5}RuO_4$ compound shows metallic density of states (13(b)) in the minority spin channel. Calculated magnetic moment at the Ru site is 1.3 μ_B which is comparable to the experimentally reported magnetic moment (22). Thus GGA+U calculations can reproduce the magnetic and electronic properties observed experimentally for these two compounds. The results suggest orthorhombic distortion is responsible for the insulating ground state in the parent compound. These GGA+U results agree well with the experimental findings.

Lattice Const. (Å)	c/a	ΔE (mRy)
a=5.4112, c=24.3271	4.4957 (-5%)	20.2
a=5.3554, c=24.8366	4.6377 (-2%)	0.7
a=5.3195, c=25.1734	4.7323 (0%)	0.0
a=5.2845, c=25.5079	4.8269 (2%)	0.9
a=5.2337, c=26.0057	4.9689 (5%)	19.5

Table 2. Lattice constants, c/a ratio and total energy difference (ΔE) between different c/a ratio structures with respect to the experimental c/a ratio structure at x=0.5.

Further, total energy calculations within GGA+U approximation for different c/a with constant volume around the critical point (x=0.5) provide some more insights. We have kept the spin configuration FM throughout as this is the ground state magnetic order reported experimentally. We then relax the cations and anions for each c/a. The lattice constants, c/a ratio and the total energy are given in Tab. 2.

We see from Fig. 13(c) that the experimental c/a has the lowest energy among all. Also, we find the metallic ground state (Fig. 13(d), (e), (f)) for all the structures. The result presented above imply that it is not possible to achieve metal insulator transition (MIT) only by changing c/a ratio, nevertheless, the system also does not have a MIT at T=0 immediately across the x=0.5. The crystal symmetry plays a crucial role here and orthogonal distortion (tilt + rotation of RuO_6 octahedra) is important to induce MIT in these compounds. This is indeed observed across x=0.2 experimentally, where system goes from tetragonal ($I4_1/acd$) to orthorhombic (S-Pbca) symmetry. GGA+U calculations also corroborate the experimental behaviour.

It is interesting to find that at x=0.5 GGA+U finds a spin-selective ferromagnetic metallic state. The direct comparison of these results with CT-QMC+DMFT and the DOS shown in Fig. 8 is difficult, since the DMFT calculation is paramagnetic and does not distinguish between majority and minority spin sectors. Nevertheless, it finds a metallic state with bad metallic features and enhanced spin fluctuations suggesting that the finite T results from this scheme are a continuation of the T=0 predictions from GGA+U. However, the quantum critical finite-T scaling collapse observed from CT-QMC+DMFT at x=0.5 does not have any analogue at T=0, and is not expected to be borne out of GGA+U finite-T extension since it depends crucially on the sampling of the correct higher order diagrams at finite T. In short, the two-techniques complement each other nicely at this interesting x=0.5 critical point, where CT-QMC+DMFT explicitly registers the critical fluctuations at finite T and GGA+U registers the correct electronic and magnetic ground state at T=0.

5. Phase Diagram for the Iso-electronic Series

All the above observations and the previous theoretical and experimental findings put together, it is reasonable to infer that the $T = 0, x = 0.5$ is a quantum critical end point separating two quasi $2D$-systems on either side, to the right, $x > 0.5$, and the left, $x < 0.5$ (Fig 14). As far as crystal structures are concerned, the $x = 2.0$ structure has higher symmetries than the one at $x = 0.0$. The dynamic in-plane susceptibility, its anisotropy and variation in the Brillouin zone at different energy scales (50; 37) also support the fact that an effective dimensional crossover attends this critical end point. Interestingly, the critical end point is also associated with a strong local ferromagnetic fluctuation extending to finite temperatures. The order of magnitude increment in local static susceptibility at this particular point of the phase diagram and the falling of (60) on both left and right side of $x = 0.5$ substantiate this view. Our findings, supported amply by experimental results, therefore, raises a relevant issue: *whether the critical point is purely structural in nature.* At this moment we would again like to rely on the detailed calculations and the results presented and infer that it is the structural change of the crystal via replacement of larger cations by smaller ones that leads to this rich structural and magnetic phase diagram. The structural changes are, therefore, the driving force behind the associated magnetic transitions and dimensional crossovers. These analyses of the microscopics of the fundamental crystal structures, rotations and hybridizations of the active bands at the Fermi level, role of dynamic correlations on those bands, their single and two-particle dynamic responses, call for a fresh look at this important series with K_2NiF_4 structure, the structural building block of another interesting unconventional superconducting series. These lead us to the phase diagram of the iso-electronic series presented in Fig 14. Finally this may also imply that the quantum critical end point of second-order structural transition would lead to a quantum critical fan, much like what is realized in high T_c superconductivity (69; 70; 71) or heavy fermion compounds (72; 73). The resulting magnetic and electronic phase diagram for

the series (Fig 14), in such a situation, will be quite interesting to explore experimentally. The paramagnetic bad metallic phase that emerges from this end point at $x = 0.5$ extends all the way to the right till $x = 2.0$ and to the left till $x = 0.0$.

At $x = 2.0$, above 25 K, the system is bad-metallic and at $x = 0.0$ the system is bad-metallic above 356 K. This implies that the critical fan would be the one connecting the end point $(x = 0.5, T = 0)$ to $x = 0.0, T = 25K$ (to the right) and $x = 2.0, T = 356K$ to the left. The iso-electronic material is a Hund's metal inside this fan, and outside it is a good metal (Fermi-liquid) below 25 K at $x = 2.0$ and magnetic (either ferro or anti-ferro) for $x < 0.5$. Only at $T = 0$, the $x > 0.5$ good-metal of 2D nature without any magnetic ground state can possibly be tuned through the $3D$ critical end point at $x = 0.5$ and render magnetically ordered (metal and insulator respectively at $0.2 < x < 0.5$ and $0 < x < 0.2$) in the region $x < 0.5$. While our studies suggest that at finite temperatures $T < 25K$ a good metal for $x > 0.5$ can be tuned inside the critical fan and made a Hund's metal that crosses the other side of the fan at $x < 0.5$ and becomes an antiferromagnetic insulator. However, the issues related to non-local, low energy fluctuations that may suppress an access to the $T = 0$, $x = 0.5$ critical end point, are hard to delineate from a local theory. Very recent experiments suggest that the $T = 0$, $x = 0.5$ point could be a cluster glass (31), which is beyond the scope of our analysis. Such a scenario, if correct, would indeed require modification of the phase diagram we have come up with: the critical fan will now end at the boundary of the cluster glass phase, and should not extend down to $T = 0$. However, inclusion of the cluster glass phase does not forbid the microscopics of the finite temperature physics of the local criticality and the critical fan sustaining a Hund's metallic phase.

6. Conclusions

The local spin fluctuation, local quantum criticality, Fermi liquidity and Hund's metallicity for the iso-electronic series $Ca_{2-x}Sr_xRuO_4$ have been addressed from a local analysis. Our systematic study of single- and two-particle features establish a comprehensive electronic and magnetic phase diagram for the iso-electronic series. We identify the critical end point at $x = 0.5, T = 0$, which acts as the vertex of a critical fan of nearly spin-frozen, non-Fermi liquid extending out in finite temperature. The critical fan suppresses the Fermi-liquid (appearing on the right) and magnetic phase (on its left). The critical point also associates a dimensional crossover and ferromagnetic spin-fluctuations.

7. Acknowledegments

SA would like to acknowledge useful discussions on the first-principles calculations with Monodeep Chakraborty. SA acknowledges discussions with Alex Hewson, J. Annett, M S Laad, C. Weber and Debraj Choudhury and thanks Arjun Mukerji for help in preparing a diagram. SA acknowledges Simons Many-Electron Collaboration, EPSRC

(grants EP/M011631/1), UGC (India) and DD acknowledges DST-Inspire (India) for research fellowships. AT acknowledges research funding from CSIR (India) through the grant number: 03(1373)/16/EMR-II.

References

[1] G. Kotliar and D. Vollhardt, Physics Today **57**, 53 (2004).

[2] E. Dagotto, Science **309**, 257 (2005).

[3] Y. Maeno and S. Nakatsuji and and S. Ikeda, Materials Science and Engineering **B 63.1** (1999): 70-75.

[4] S. G. Ovchinnikov, Physics-Uspekhi **46**, 21 (2003).

[5] Z. Yin and K. Haule and G. Kotliar, Nature materials **10**, 932 (2011).

[6] K. Haule and G. Kotliar, New journal of physics **11**, 025021 (2009).

[7] L. Sun *et al.*, Nature **483.7387**, 67-69 (2012).

[8] I. Okada, K. Yosida, Prog. Theor. Phys. **49**:14831502 (1973).

[9] C. Jayaprakash and H. Krishna-Murthy and J. Wilkins, Physical Review Letters **47**, 737 (1981).

[10] B. Jones and C. Varma, Physical Review letters **58**, 843 (1987).

[11] H. Kusunose and K. Miyake, Journal of the Physical Society of Japan **66**, 1180 (1997).

[12] T. Pruschke and R. Bulla, The European Physical Journal B-Condensed Matter and Complex Systems **44**, 217 (2005).

[13] J. Mravlje and M. Aichhorn and T. Miyake and K. Haule and G. Kotliar and A. Georges, Physical review letters **106**, 096401 (2011).

[14] L. de' Medici, arXiv preprint arXiv 1707.03282

[15] H. T. Dang and J. Mravlje and A. Georges and A. J. Millis, Physical Review B **91**, 195149 (2015).

[16] X. Deng and K. Haule and G. Kotliar, arXiv preprint arXiv:1504.00292 (2015).

[17] J. Rincón and A. Moreo and G. Alvarez and E. Dagotto, Physical Review B **90**, 241105 (2014).

[18] M. Kim and B. Min, Physical Review B **91**, 205116 (2015).

[19] Q. Han and H. T. Dang and A. Millis, Physical Review B **93**, 155103 (2016).

[20] N. Dasari and S. Yamijala and S. K. Pati and M. Jain and T. S. Dasgupta and J. Moreno and M. Jarrell and N. Vidhyadhiraja, arXiv preprint arXiv:1511.01371 (2015).

[21] A. Steppke *et al.*, arXiv preprint arXiv:1604.06669 (2016).

[22] M. Braden and G. Andre and S. Nakatsuji and Y. Maeno, Physical Review B **58**, 847 (1998).

[23] C. Alexander and G. Cao and V. Dobrosavljevic and S. McCall and J. Crow and E. Lochner and R. Guertin, Physical Review B **60**, R8422 (1999).

[24] J. Mravlje and A. Georges, arXiv preprint arXiv:1504.03860 (2015).

[25] S. Acharya and M. S. Laad and D. Dey and T. Maitra and A. Taraphder, Scientific Reports 7, 43033 (2017)

[26] M. Kim and J. Mravlje and M. Ferrero and O. Parcollet and A. Georges arXiv preprint arXiv:1707.02462

[27] E. Gorelov and M. Karolak and T. O. Wehling and F. Lechermann and A. I. Lichtenstein and E. Pavarini, Phys. Rev. Lett. **104**, 226401 (2010).

[28] D. Stutter *et al.*, Nature Communications 8:15176, (2017).

[29] G. Khaliullin, Physical review letters **111**, 197201 (2013).

[30] O. Friedt and M. Braden and G. André and P. Adelmann and S. Nakatsuji and Y. Maeno, Physical Review B **63**, 174432 (2001).

[31] J. Carlo *et al.*, Nature materials **11**, 323 (2012).

[32] Philipp Werner, Armin Comanac, Luca de Medici, Matthias Troyer, and Andrew J. Millis, Phys. Rev. Lett. 97, 076405 (2006).

[33] Emanuel Gull, Andrew J. Millis, Alexander I. Lichtenstein, Alexey N. Rubtsov, Matthias Troyer, and Philipp Werner, Rev. Mod. Phys. 83, 349 (2011).

[34] Bauer, B. *et al.* The alps project release 2.0: open source software for strongly correlated systems. *Journal of Statistical Mechanics: Theory and Experiment* **2011**, P05001 (2011).

[35] P. Blaha and K. Schwarz and G. Madsen and D. Kvasnicka and J. Luitz, An augmented plane wave+ local orbitals program for calculating crystal properties (2001).

[36] M. Braden, H. Moudden, S. Nishizaki, Y. Maeno, T. Fujita, Physica C **273**, 248 (1997).

[37] S. Nakatsuji and Y. Maeno, Physical Review B **62**, 6458 (2000).

[38] A. A. Mostofi and J. R. Yates and Y.-S. Lee and I. Souza and D. Vanderbilt and N. Marzari, Computer physics communications **178**, 685 (2008).

[39] J. Kuneš and R. Arita and P. Wissgott and A. Toschi and H. Ikeda and K. Held, Computer Physics Communications **181**, 1888 (2010).

[40] S. Raghu and A. Kapitulnik and S. Kivelson, Physical review letters **105**, 136401 (2010).

[41] A. Damascelli *et al.*, Physical review letters **85**, 5194 (2000).

[42] G. Zhang and E. Gorelov and E. Sarvestani and E. Pavarini, Physical review letters **116**, 106402 (2016).

[43] Q. Han, H. T. Dang, and A. J. Millis Phys. Rev. B 93, 155103 (2016).

[44] T. Schäfer and G. Rohringer and O. Gunnarsson and S. Ciuchi and G. Sangiovanni and A. Toschi, Phys. Rev. Lett. **110**, 246405 (2013).

[45] D. E. Logan and A. P. Tucker and M. R. Galpin, Phys. Rev. B **90**, 075150 (2014).

[46] P. Werner and E. Gull and M. Troyer and A. J. Millis, Phys. Rev. Lett. **101**, 166405 (2008).

[47] A. Koga and N. Kawakami and T. M. Rice and and M. Sigrist, Phys. Rev. B **72**, 045128 (2005).

[48] Y. Maeno, S. Kittaka, T. Nomura, S. Yonezawa, and K. Ishida, J. Phys. Soc. Jpn. 81, 011009 (2012).

[49] A. P. Mackenzie and Y. Maeno, Reviews of Modern Physics **75**, 657 (2003).

[50] Z. Fang and N. Nagaosa and K. Terakura, Physical Review B **69**, 045116 (2004).

[51] Z. Fang and K. Terakura, Physical Review B **64**, 020509 (2001).

[52] Jarrell, M. Jarrell and J. E. Gubernatis, Phys. Rep. **269**, 133 (1996).

[53] S. Kirchner and Q. Si, Physical review letters **100**, 026403 (2008).

[54] N. Dasari and S. Acharya and A. Taraphder and J. Moreno and M. Jarrell and N. Vidhyadhiraja, arXiv preprint arXiv:1509.09163 (2015).

[55] K. Ingersent and Q. Si, Physical review letters **89**, 076403 (2002).

[56] S. Acharya and M. Laad and A. Taraphder, arXiv preprint arXiv:1602.08990 (2016).

[57] S. Acharya and M. Laad and A. Taraphder, arXiv preprint arXiv:1603.09126 (2016).

[58] M. Uruma et al., arXiv: 0711.2160 (2007).

[59] S. C. Wang et al., Phys. Rev. Lett. 93, 177007 (2004).

[60] S. Nakatsuji and Y. Maeno, Physical review letters **84**, 2666 (2000).

[61] F. Nakamura, R. Nakai, T. Takemoto, M. Sakaki, T. Suzuki, P. L. Alireza, S. Nakatsuji, and Y. Maeno, Phys. Rev. B 80, 193103 (2009).

[62] P. L. Alireza et al., Journal of Physics: Condensed Matter, Volume 22, Number 5.

[63] V. Anisimov and I. Nekrasov and D. Kondakov and T. Rice and M. Sigrist, The European Physical Journal B-Condensed Matter and Complex Systems **25**, 191 (2002).

[64] M. Neupane and P. Richard and Z.-H. Pan and Y.-M. Xu and R. Jin and D. Mandrus and X. Dai and Z. Fang and Z. Wang and H. Ding, Physical review letters **103**, 097001 (2009).

[65] A. Shimoyamada and K. Ishizaka and S. Tsuda and S. Nakatsuji and Y. Maeno and S. Shin, Physical review letters **102**, 086401 (2009).

[66] I. Zegkinoglou *et al.*, Physical review letters **95**, 136401 (2005).

[67] J. Jung and Z. Fang and J. He and Y. Kaneko and Y. Okimoto and Y. Tokura, Physical review letters **91**, 056403 (2003).

[68] T. Hotta and E. Dagotto, Physical review letters **88**, 017201 (2001).

[69] S. Sachdev, physica status solidi (b) **247**, 537 (2010).

[70] J.-H. Chu and J. G. Analytis and C. Kucharczyk and I. R. Fisher, Physical Review B **79**, 014506 (2009).

[71] N. Ni and A. Thaler and A. Kracher and J. Yan and S. Budko and P. Canfield, Physical Review B **80**, 024511 (2009).

[72] N. Mathur and F. Grosche and S. Julian and I. Walker and D. Freye and R. Haselwimmer and G. Lonzarich, Nature **394**, 39 (1998).

[73] Q. Si and S. Paschen, physica status solidi (b) **250**, 425 (2013).

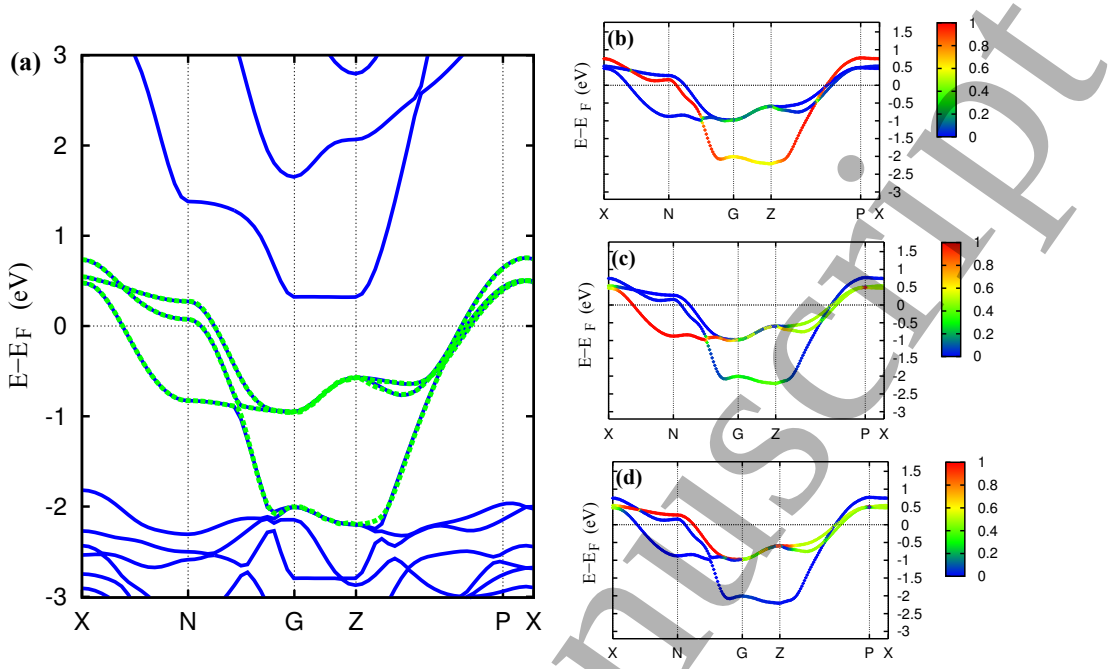

Figure 1. (color online) Left panel: Band structure (blue solid lines) for Sr_2RuO_4 within GGA and Wannier fitting (green dotted lines) for the bands crossing the Fermi level. Right panel: Band characterization of the Wannier fit bands for Sr_2RuO_4. The contribution of the d_{xy}, d_{xz} and d_{yz} Wannier orbitals to the fitted bands are shown in (b), (c) and (d)respectively through the color codes. Highest contribution is color red and blue stands for the lowest.

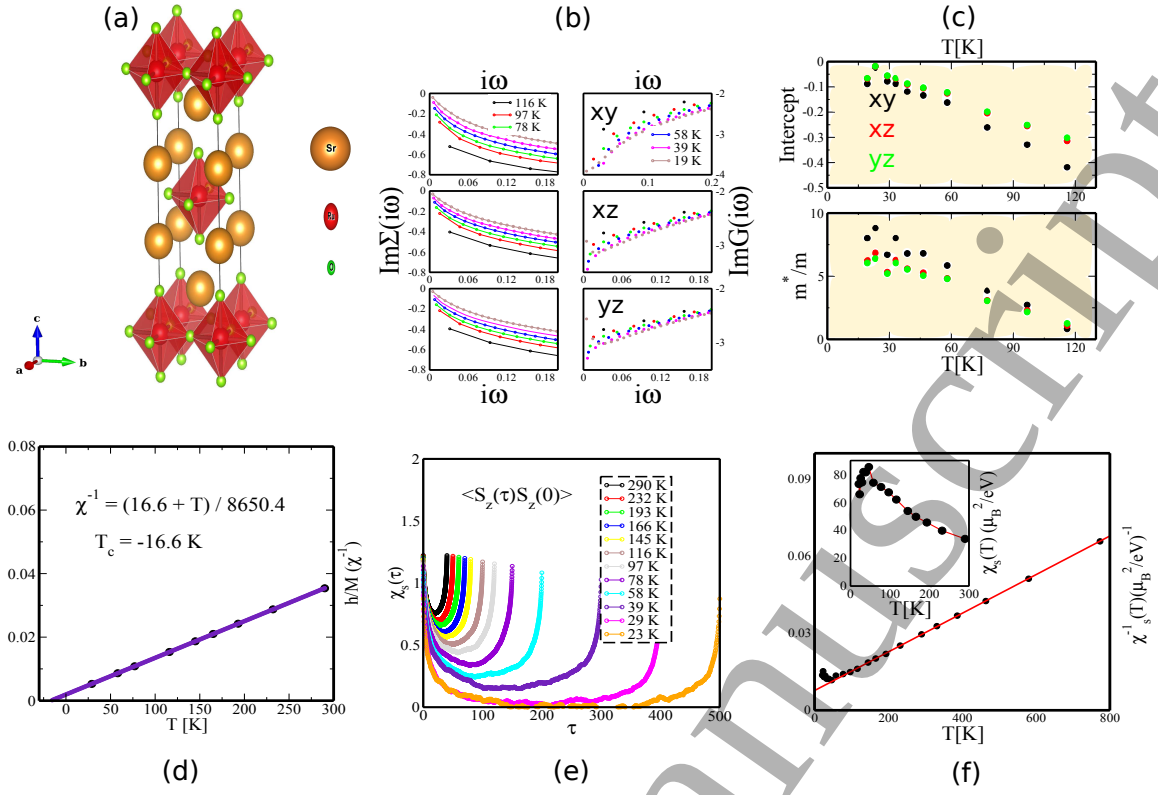

Figure 2. (a) Crystal structure of Sr_2RuO_4 with (space-group I4/mmm) tetragonal structure (a=3.8606 A^0 and c=12.70658 A^0). (b) The Im$\Sigma(i\omega)$ and Im$G(i\omega)$ for three orbitals (d_{xy}, d_{xz}, d_{yz}) over a range of temperatures show retrieval of coherence at lower temperatures. (c) The intercepts of Im$\Sigma(i\omega)$ at ω=0 and the renormalized mass enhancement factors m^*/m are shown for a large range of temperatures (here m is bare mass at DFT level). (d) The inverse of the uniform spin susceptibility ($\chi^{-1} = h/M$) as a function of temperature is plotted between 290 K and 29 K. The critical temperature (T_c) for the magnetic transition for Sr_2RuO_4 T_c is found from a Curie-Weiss fit to be -16.6 K, indicating pre-dominant anti-ferromagnetic spin fluctuations. (e) The dynamic local spin susceptibilities ($\chi_s(\tau)$) over a range of temperatures show the tendency towards retrieval of a low temperature Fermi-liquid phase. (f) $\chi_s^{-1}(T)$ as a function of temperature shows the low temperature Fermi-liquid phase sets in at $\sim 41K$, where the nature of the susceptibility deviates from Curie-Weiss behavior. The low temperature features of the spin susceptibility in inset is zoomed in to show the temperature scale at which this deviation takes place.

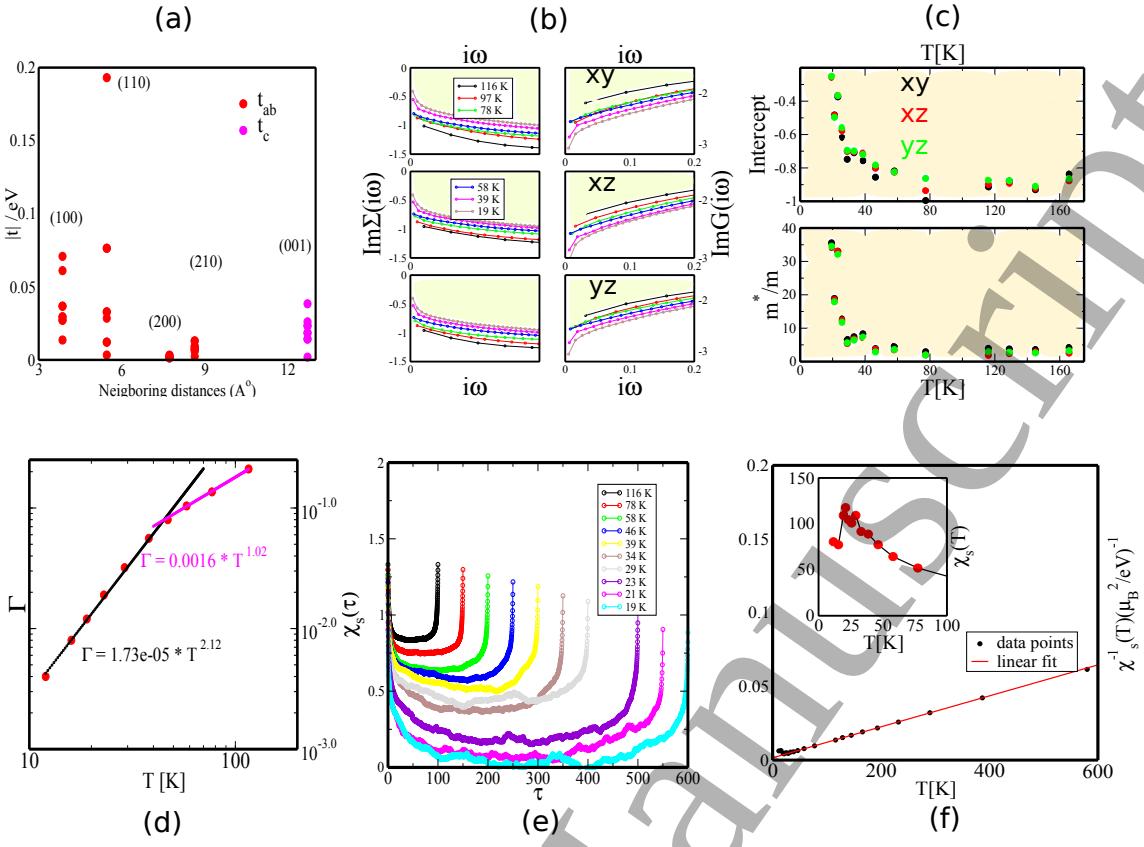

Figure 3. (a) The in-plane (t_{ab}) and out of plane (t_c) hopping elements for Sr_2RuO_4, extracted from real space Wannier hopping matrix showing the $2D$ electron itinerant nature (a=3.8606 A^0 and c=12.70658 A^0) (b) The Im$\Sigma(i\omega)$ and Im$G(i\omega)$ for three orbitals (d_{xy}, d_{xz}, d_{yz}) are shown over a range of temperatures. (c) The intercepts of Im$\Sigma(i\omega)$ at ω=0 and the renormalized mass enhancement factors m^*/m show orbital specific retrieval of coherence at low temperatures (here m is bare mass at DFT level). (d) The scattering rate Γ crosses over from a high temperature linear thermal exponent to a lower temperature quadratic thermal exponent. This clearly marks the advent of a FL like phase at lower temperatures. (e) $\chi_s(\tau)$ for a range of temperatures show tendency towards retrieval of a low temperature Fermi-liquid phase. (f) $\chi_s^{-1}(T)$ shows the low temperature Fermi-liquid phase sets in at $\sim 23K$, where the nature of the susceptibility deviates from Curie-Weiss behavior. The inset shows the spin susceptibility zoomed in at low temperatures, clearly showing the emergence of coherence at $\sim 23K$.

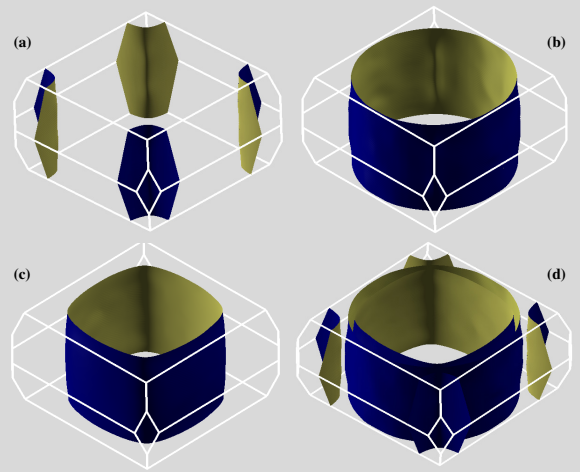

Figure 4. The Fermi surfaces of Sr_2RuO_4 for (a) d_{xz} (b) d_{xy} (c) d_{yz} orbitals and (d) for the total system. It is interesting to note that d_{xz} and d_{yz} Fermi surfaces are effectively one dimensional and d_{xy} Fermi surface is two dimensional, making the whole system quasi 2D.

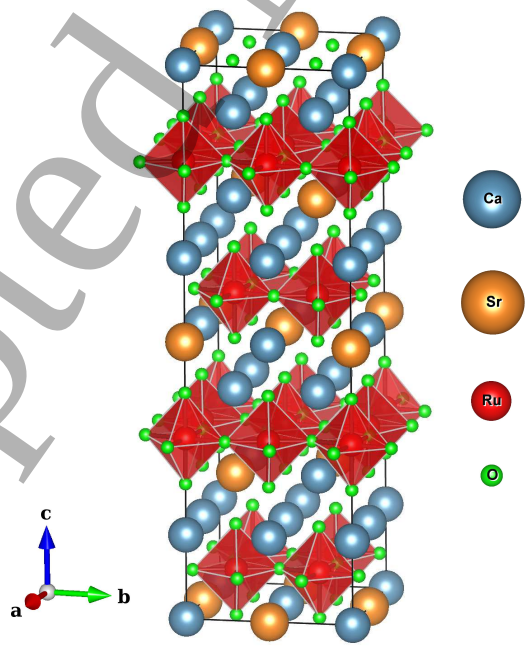

Figure 5. The tetragonal crystal structure of $Ca_{1.5}Sr_{0.5}RuO_4$ (space-group $I4_1/acd$, a=7.52 A^0 and c=24.1645 A^0).

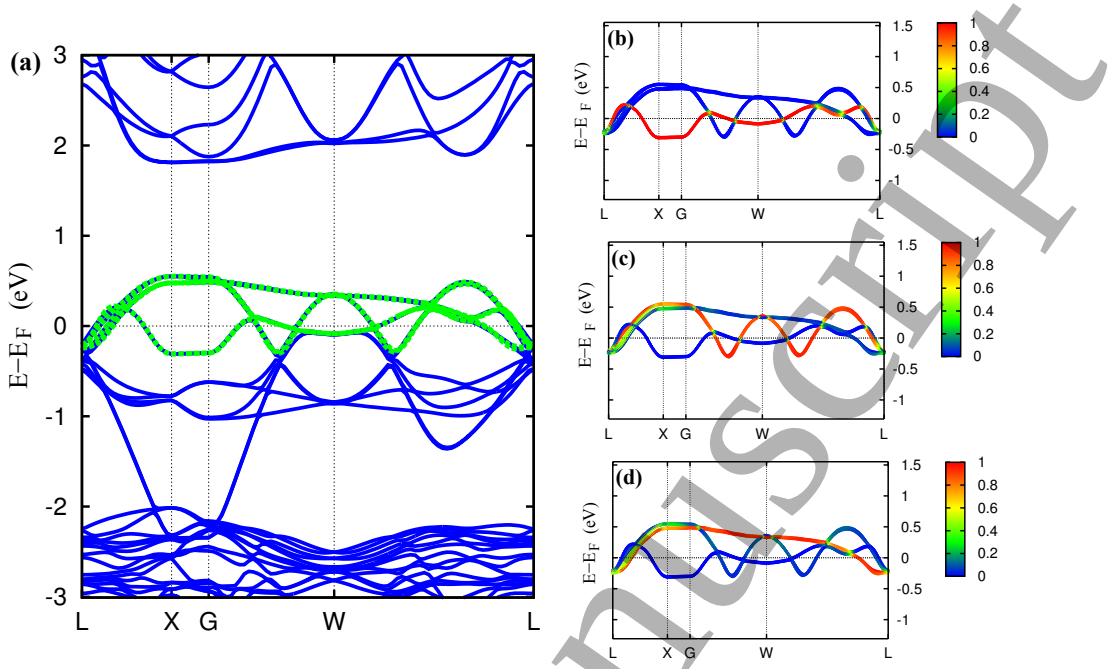

Figure 6. (left panel) Band structure (blue solid lines) for $Ca_{1.5}Sr_{0.5}RuO_4$ within GGA and Wannier fitting (green dotted lines) for the bands crossing the Fermi level. (right panel) Band characterization of the Wannier fit bands for $Ca_{1.5}Sr_{0.5}RuO_4$. The contribution of the d_{xy}, d_{xz} and d_{yz} Wannier orbitals to the fitted bands are shown in (b), (c) and (d)respectively.

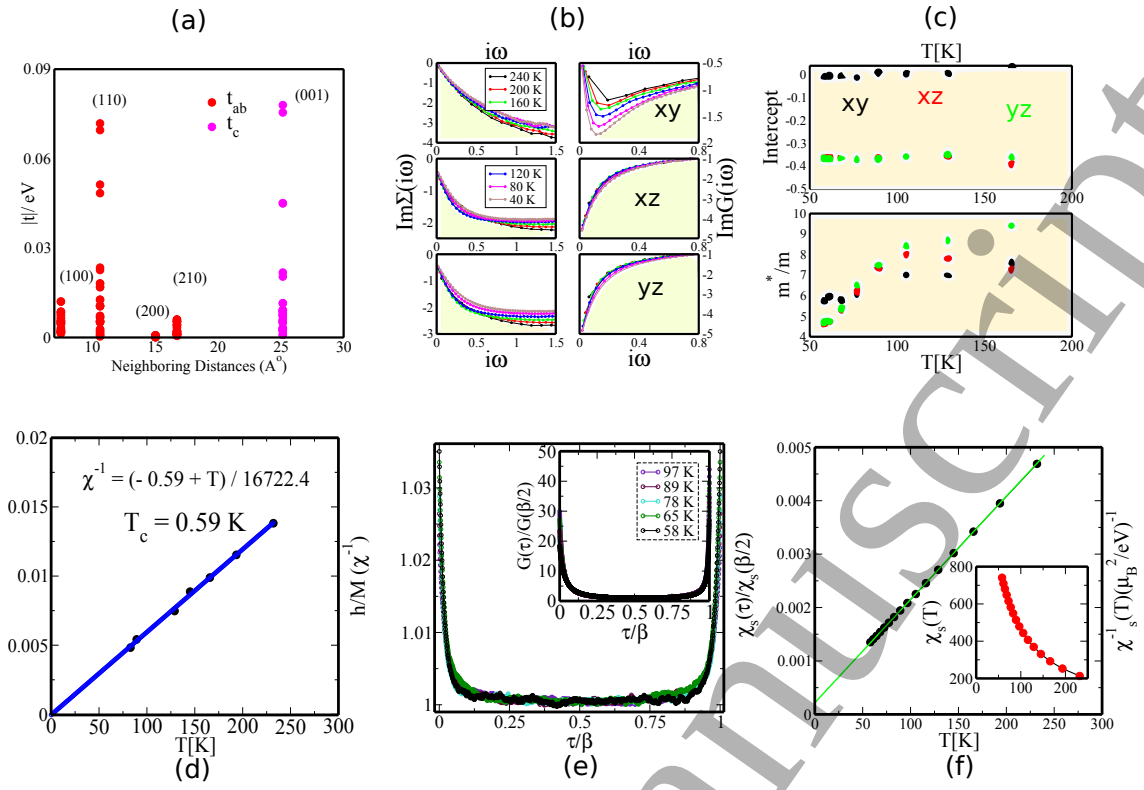

Figure 7. (a) The in-plane (t_{ab}) and out of plane (t_c) hopping elements for $Ca_{1.5}Sr_{0.5}RuO_4$, extracted from real space Wannier hopping matrix showing the $3D$ electron itinerant nature. (b) The Im$\Sigma(i\omega)$ and Im$G(i\omega)$ for three orbitals (d_{xy}, d_{xz}, d_{yz}) are shown over a range of temperatures. (c) The intercepts of Im$\Sigma(i\omega)$ at ω=0 and the renormalized mass enhancement factors m^*/m shows orbital selective coherence for a large range of temperatures (m is bare mass at DFT level). (d) The inverse of uniform spin susceptibility ($h/M(\chi^{-1})$) as a function of temperature is shown with Curie-Weiss fitting ($\frac{h}{M} \sim (T - T_c)$). The critical temperature (T_c) for the magnetic transition is positive 0.59 K. (e) The scaled dynamic spin susceptibilities ($\chi_s(\tau)/\chi_s(\beta)$) for a range of temperatures show perfect scaling collapse as functions of τ/β. The strong thermal scaling collapse is also evident from $G(\tau)/G(\beta/2)$ as shown in inset. (f) The inverse of local static spin susceptibility $\chi_s^{-1}(T)$ shows that the system has Curie-Weiss spin response down to the lowest accessible temperatures. The inset zooms in the low temperature response for $\chi_s(T)$ confirming the same. Also the magnitude of the susceptibilities is substantially enhanced at this point.

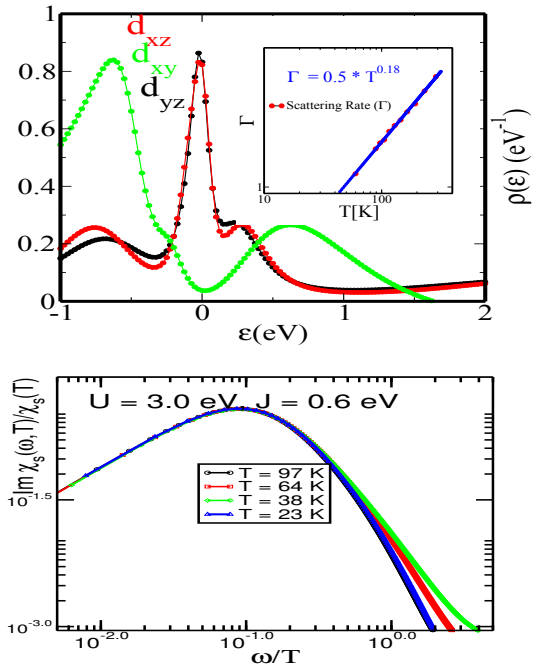

Figure 8. (Upper Panel) The analytically continued local orbitally projected DOS for $Ca_{1.5}Sr_{0.5}RuO_4$, clearly shows the quasiparticle excitation in d_{xz}, d_{yz} channels, while the d_{xy} channel is pseudogapped. In the inset we show the scattering rate Γ (as derived from the intercept of the -Im$\Sigma(\omega = 0)$ as a function of temperature. We find that the scattering rate has a thermal exponent 0.18, which is far from the quadratic Fermi liquid limit. (Lower Panel) The local dynamic spin susceptibilities $(\chi_s(\tau))$ are analytically continued using maximum entropy method. On thermal scaling the curves $(\mathrm{Im}\chi_s(\omega, T)/\chi_s(T))$ over a range of temperature have perfect collapse on each other upto ω/T ~1.0. The local dynamic spin susceptibilities $(\chi_s(\tau))$ are analytically continued using maximum entropy method. On thermal scaling the curves $(\mathrm{Im}\chi_s(\omega, T)/\chi_s(T))$ over a range of temperature have perfect collapse on each other upto ω/T ~1.0.

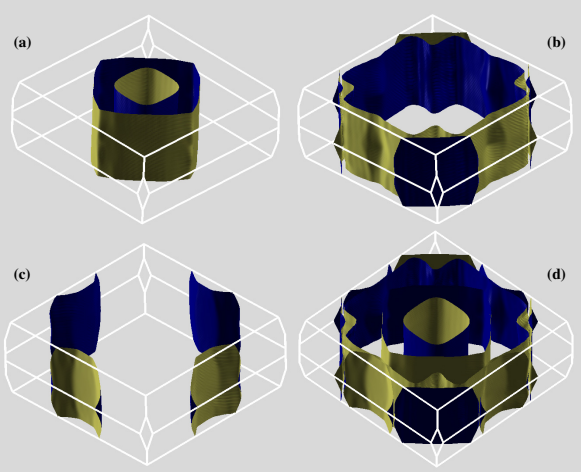

Figure 9. The Fermi surfaces of $Ca_{1.5}Sr_{0.5}RuO_4$ for (a) d_{xz} (b) d_{xy} (c) d_{yz} orbitals and (d) for the total system. It is interesting to note that unlike the Sr_2RuO_4 these Fermi surfaces for $x = 0.5$ have significant dispersion along the z direction.

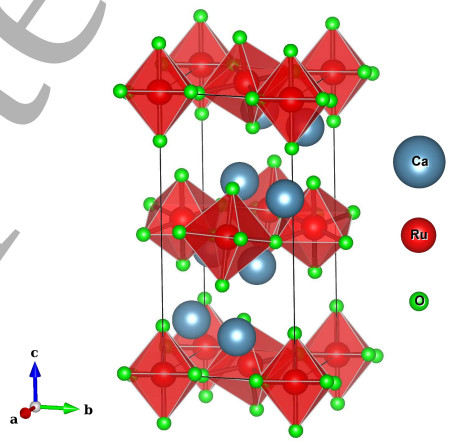

Figure 10. Crystal structure of Ca_2RuO_4 with L-Pbca structure a=5.3869 A^0, b=5.6334 A^0, c=11.7349 A^0.

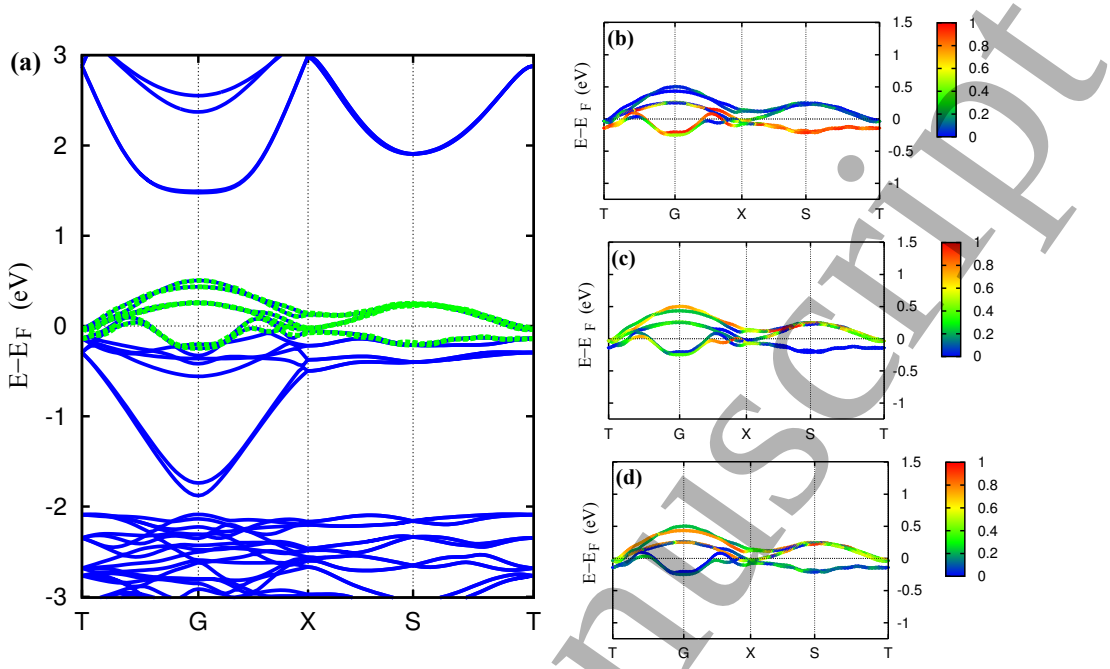

Figure 11. (left panel) Band structure (blue solid lines) of Ca_2RuO_4 within GGA and the corresponding Wannier fitting (green dotted lines) for the bands crossing the Fermi level. (right panel) Band characterization of the Wannier fit bands for Ca_2RuO_4. The contribution of the d_{xy}, d_{xz} and d_{yz} Wannier orbitals to the fitted bands are shown in (b), (c) and (d)respectively.

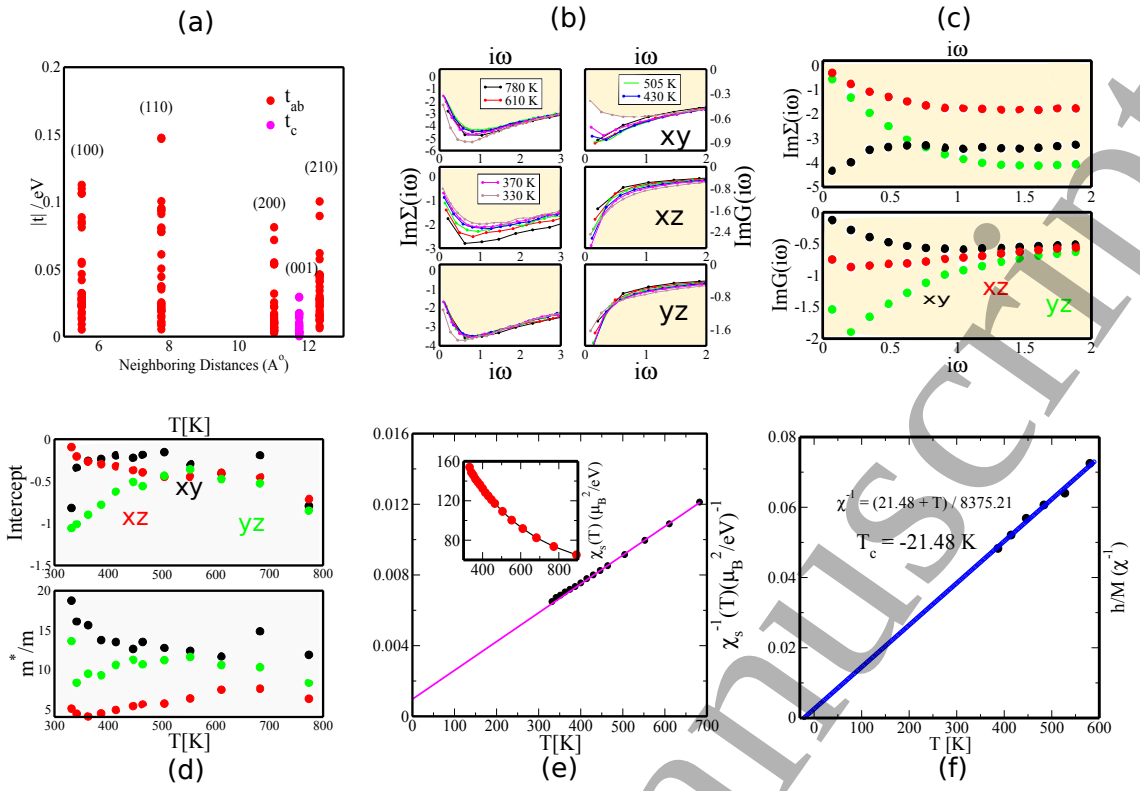

Figure 12. (a) The in-plane (t_{ab}) and out of plane (t_c) hopping elements for Ca_2RuO_4, extracted from real space Wannier hopping matrix showing $2D$ nature of the itinerant electrons. (b) The Im$\Sigma(i\omega)$ and Im$G(i\omega)$ for three orbitals (d_{xy}, d_{xz}, d_{yz}) are shown over a range of temperatures. (c)The Im$\Sigma(i\omega)$ and Im$G(i\omega)$ for three orbitals (d_{xy}, d_{xz}, d_{yz}) are shown at 250 K showing orbital selective Mott transition. (d) The intercepts of Im$\Sigma(i\omega)$ at ω=0 and the renormalized mass enhancement factors m^*/m are shown for a large range of temperatures (m is bare mass at DFT level). (e) The main panel and the inset clearly shows that $\chi_s(T)$ has Curie-Weiss features. (f) The inverse of uniform spin susceptibility (h/M) is fitted to the form $\sim (T - T_c)$. The Curie-Weiss temperature T_c is negative (-21.48 K) here, showing that the predominant fluctuation of the material is antiferromagnetic.

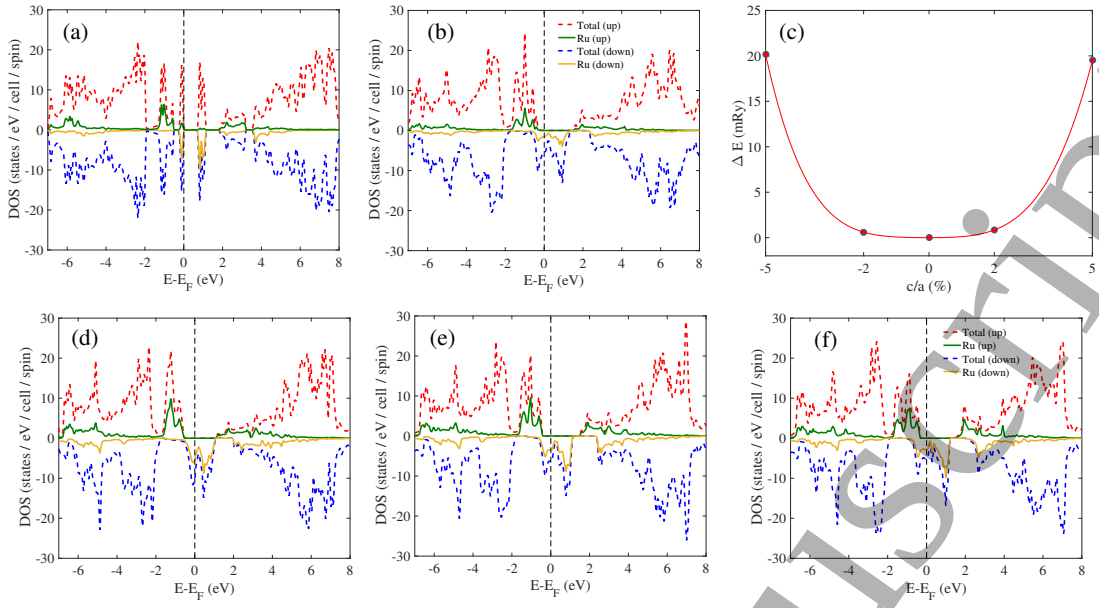

Figure 13. (Color online) Spin-polarized DOS are shown for (a) x=0 (AFM spin configuration) and (b) x=0.5 (FM spin configuration). Green and yellow solid lines represent partial DOS of Ru in majority (up) and minority (down) spin channel respectively. (c) Energy difference plot for different c/a ratio structures with respect to the experimental c/a ratio structure at x=0.5. Spin-polarized DOS are shown for x=0.5 structure with different c/a ratio (d) -5%, (e) 0%, (f) 5% with respect to experimental structures. Green and yellow solid lines represent partial DOS of Ru in majority (up) and minority spin (down) channel respectively.

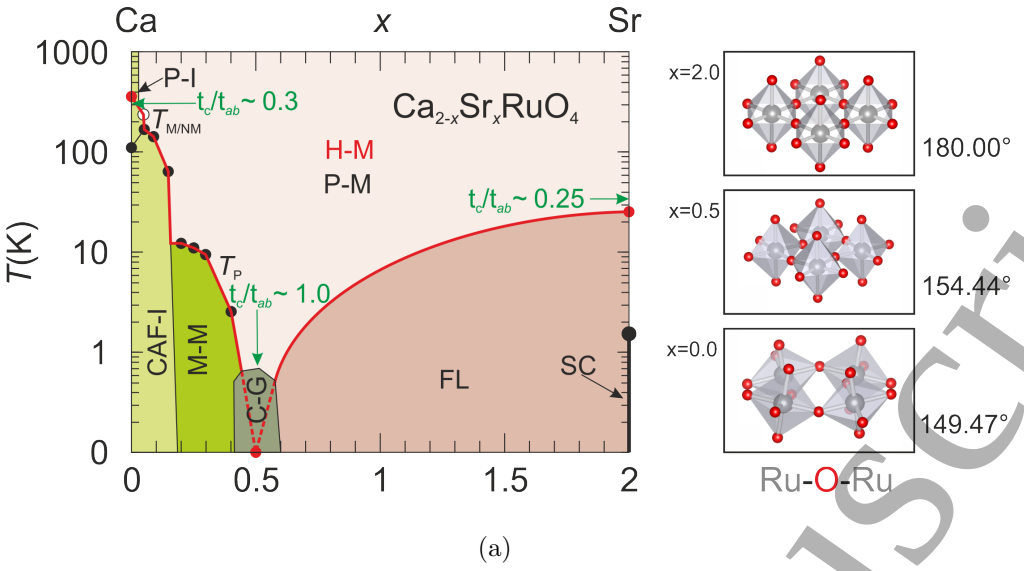

(a)

Figure 14. Modified magnetic and electronic phase diagram for $Ca_{2-x}Sr_xRuO_4$ showing critical dimensional crossover across $x = 0.5$. The ratio of t_c/t_{ab} across the phase diagram explicitly shows the aspects of structural criticality at $x = 0.5$. A Hund's metallic phase spans the quantum critical regime at finite T and finite x emanating from $T = 0, x = 0.5$ end point. The enhanced magnitude of local moment and ferromagnetic spin fluctuation associate the critical end point. The critical fan suppresses a low temperature Fermi liquid phase to the right $x > 0.5$ and a magnetically order phase to its left $x < 0.5$. The octahedral distortions across the phase diagram and $Ru - O - Ru$ bond-angles are shown in the panel on the right side.